ALMA MATER STUDIORUM
UNIVERSITÀ DI BOLOGNA
CESENA CAMPUS

DEPARTMENT OF ELECTRICAL ENERGY AND
INFORMATION ENGINEERING "GUGLIELMO MARCONI"
Second Cycle Degree in Biomedical Engineering for Neuroscience

"AN OPEN-SOURCE MODULAR PIPELINE FOR SPINAL CORD SEGMENTATION FROM MAGNETIC RESONANCE IMAGING"

Thesis in
Neuro-robotics and Neurorehabilitation

Thesis by:
MARCO EGIDIO RESSA

Supervisor:
Prof. Eng.
CRISTIANO CUPPINI
Co-Supervisor:
Dr.
SIMONE ROMENI

SESSION VI
ACADEMIC YEAR 2024-2025

Keywords

Spinal Cord Injury

Spinal Cord Toolbox

SpinePS

TotalSegmentator

TotalSpineSegmentator

Contents

Abstract

The simulation of spinal cord electrical stimulation using finite element models requires anatomically coherent three-dimensional geometries, as the distribution of the electric field depends sensitively on cord morphology and on the thickness of the perimedullary compartment. In this work, a computational pipeline was developed for the construction of spinal compartments from multi-contrast MRI images (T2-weighted and T2*-weighted), applied to a multicenter open-access dataset. Spinal cord and intramedullary compartment segmentation was performed using Spinal Cord Toolbox and integrated with registration to the PAM50 template, in order to obtain masks of cord, gray matter, white matter, and cerebrospinal fluid consistent within the subject's anatomical space. Vertebral structures were segmented separately, generating complete geometric configurations within the same reference system, ready for use in electrophysiological simulations. In parallel, a comparative analysis was conducted among three automatic segmentation toolboxes (SpinePS, TotalSegmentator and TotalSpineSegmentator) applied to the same T2-weighted images. For each model, geometric parameters derived from the native spinal cord segmentation were computed, including total volume, cranio-caudal length, mean cross-sectional area, and vertebral canal-to-cord ratio. The comparison highlights systematic differences in the definition of anatomical boundaries across frameworks, resulting in variations in morphometric metrics. The results emphasize that the choice of segmentation algorithm represents a relevant methodological variable in the construction of geometries for numerical modeling. The proposed approach provides a reproducible procedure for generating spinal models intended for electrical stimulation simulations and, at the same time, a quantitative assessment of the influence of automatic segmentation tools on the geometric quantities employed in FEM models.

Chapter 1

Introduction

Spinal cord injury (SCI) encompasses a heterogeneous group of conditions characterized by structural and functional alterations of spinal cord tissue [1, 2]. From an epidemiological perspective, the Global Burden of Disease Study 2021 estimates that approximately 574,000 new cases occurred worldwide in 2021 alone and that about 15 million people are living with the consequences of SCI [1, 3]. The average annual incidence generally ranges between 20 and 30 cases per million inhabitants, with marked geographical variability related to demographic and socioeconomic factors [3, 4]. Traumatic forms, associated with acute mechanical events such as road traffic accidents or falls, are distinguished from non-traumatic forms related to neoplasms, degenerative processes, or inflammatory conditions [5, 3]. Incidence is higher in males and tends to increase with age [1, 3, 4]. Clinically, injury severity is classified according to the anatomical level and the degree of neurological impairment based on the International Standards for Neurological Classification of Spinal Cord Injury (ISNCSCI) [6]. The level determines the distribution of motor and sensory deficits, whereas the distinction between complete and incomplete injury depends on the presence of residual function below the affected segment. In sublesional segments, despite the absence of suprasegmental control, anatomical structures remain macroscopically present [2], as illustrated in Figure 1.1.

Over the past two decades, neuromodulation strategies such as epidural and transcutaneous stimulation have demonstrated the possibility of modulating the excitability of sublesional spinal circuits and partially restoring motor functions [7, 8, 9, 10, 11]. In these approaches, stimulation efficacy does not depend exclusively on stimulus parameters and electrode configuration, but also on tissue geometry and on the thickness of the cerebrospinal fluid layer separating the electrodes from the cord [12]. Computational models based on the Finite Element Method (FEM) represent a well-established

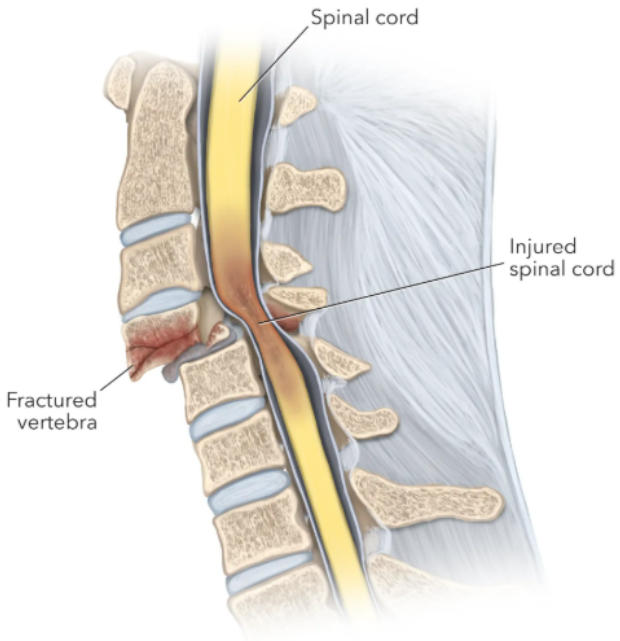

Figure 1.1: Schematic representation of spinal cord injury (SCI).

tool for estimating extracellular potential distribution and predicting neural structure activation [13, 14, 15, 16, 17]. In such models, the electric field distribution is highly sensitive to the geometric definition of anatomical compartments and to the conductivity properties assigned to gray matter, white matter, and cerebrospinal fluid. Variations in spinal cord cross-sectional area or in the thickness of the perimedullary compartment may lead to significant changes in the simulated field [13]. Consequently, the quality of anatomical segmentation constitutes a critical methodological variable in the construction of geometries for numerical modeling. The use of convolutional neural networks has fostered the development of automatic tools for spinal cord segmentation on MRI images, integrated into open-source frameworks [18, 19, 20]. Although such tools show high performance according to spatial overlap metrics [18], differences in the operational definition of anatomical boundaries may translate into variations in morphometric quantities relevant for modeling [21]. The impact of toolbox selection on the geometric metrics used in spinal electrophysiological models remains, however, insufficiently explored. In the present study, a reproducible pipeline is developed for the segmentation of the healthy spinal cord from multi-contrast MRI images, aimed at generating geometrically coherent three-dimensional models for FEM simulations of stimulation in macroscopically preserved sublesional segments of

SCI. In parallel, a comparative analysis is conducted among three automatic segmentation toolboxes (SpinePS, TotalSegmentator and TotalSpineSegmentator) to assess variability in the main spinal morphometric metrics derived from their respective segmentations. The inter-site and inter-scanner variability of the reference dataset is illustrated in Figure 1.2.

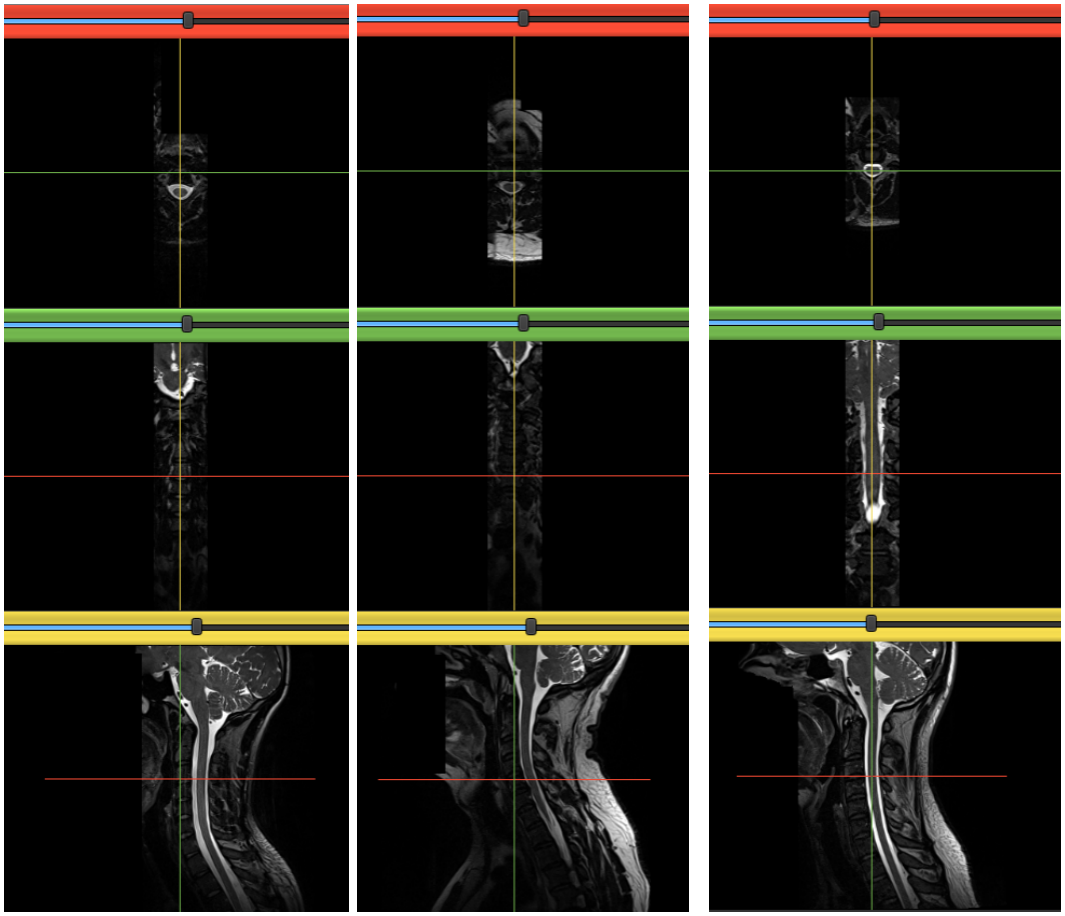

Figure 1.2: Example of inter-site variability in T2-weighted spinal cord MRI acquired at different imaging centers.

Chapter 2

Materials and Methods

2.1 Dataset

The images used in the present study were obtained from the Spine Generic Public Database in the Multi-Subject configuration [22], an open-access dataset acquired according to the Spine Generic protocol and organized according to the Brain Imaging Data Structure (BIDS) standard [23]. The BIDS structure defines a subject/session/contrast hierarchy and associates each volume with JSON files containing acquisition metadata, ensuring image traceability and reproducibility of the analyses. Only healthy adult subjects not listed in the official `exclude.yml` file were included. The exclusion criteria reported in the aforementioned file include, among the main causes, the presence of motion artifacts and non-compliance with the acquisition parameters specified by the Spine Generic protocol. As an example, subject `sub-balgrist01` was excluded due to evident motion artifacts in the T1-weighted images, characterized by distortions and alterations of anatomical contours (Figure 2.1). Similarly, subject `beijingVerio01` was excluded because the acquisition site did not adhere to the parameters defined in the shared protocol, reporting non-compliant repetition time (TR = 2 ms) and flip angle (FA = 180°) values (Figure 2.2).

The dataset was downloaded using `git` and `git-annex`, preserving its original structure in its entirety. For the purposes of this study, structural T2-weighted (T2w) and T2*-weighted (T2*w) sequences were used. All processing steps were performed in the subject's native T2w space, adopted as the common anatomical reference, in order to avoid repeated interpolations and ensure geometric consistency across compartments.

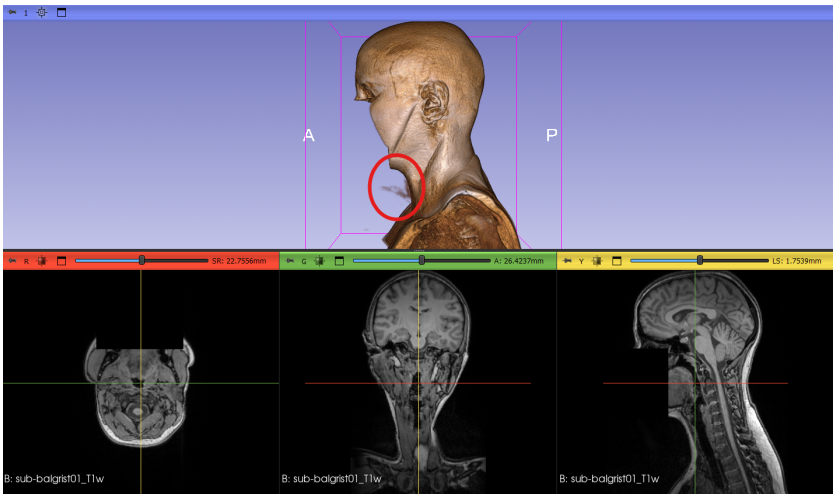

Figure 2.1: Motion artifact in `sub-balgrist01`.

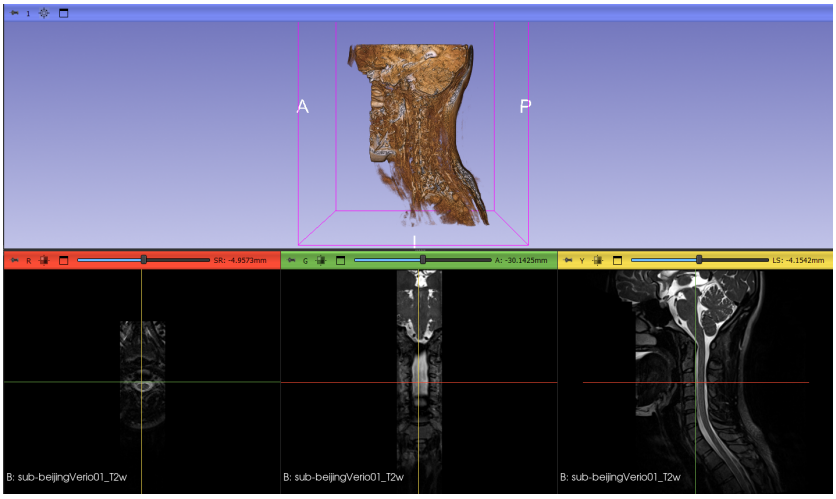

Figure 2.2: Non-compliance with protocol in `beijingVerio01`.

2.2 Spinal Cord Segmentation and Registration to PAM50

Initial spinal cord segmentation was performed using Spinal Cord Toolbox (SCT, version 7.0) [19]. The cord contour was obtained on T2w images using the pre-trained model for this contrast (`sct_deepseg_sc`). The resulting mask and the associated centerline were used as structural constraints during registration to the PAM50 template. In particular, the availability of the spinal cord segmentation allows the non-linear registration procedure to constrain alignment along the cranio-caudal axis, reducing local distortions and improving correspondence between vertebral levels. Gray matter (GM) was segmented on T2w images using `sct_deepseg_gm`, exploiting the higher intramedullary contrast of this sequence. White matter (WM) was computed by logical subtraction from the full spinal cord mask segmented in the same T2w space, thereby ensuring topological consistency between compartments. The GM and WM masks were subsequently mapped into T2w space through inter-contrast registration, so that all intramedullary compartments were expressed within the same geometric reference system (see Figure 2.3).

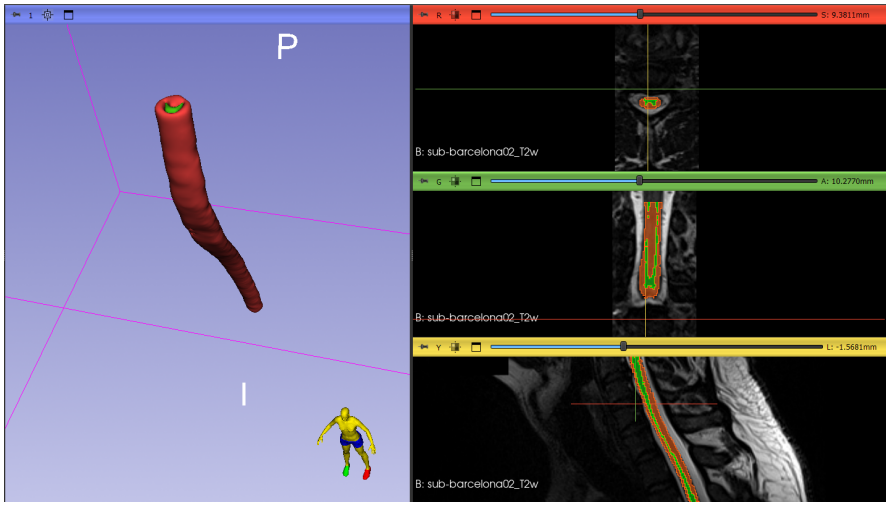

Figure 2.3: Spinal cord segmentation on T2w images and gray matter segmentation on T2*w images, with white matter derived by logical subtraction.

Registration to the PAM50 template was then performed using `sct_register_to_template`, with the T2w image and the spinal cord segmentation provided as inputs. The C2–C3 intervertebral disc was manually identified to initialize vertebral labeling, a necessary condition to stabilize alignment along the spinal axis. The procedure generated both the

forward transformation (subject→template) and the inverse transformation (template→subject). In the present study, the inverse transformation was used to map the PAM50 template cord and gray matter into the subject's native T2w space. The use of the template-derived cord mapped into individual space enables the reconstruction of a continuous and geometrically coherent spinal cord along the entire cranio-caudal axis, reducing the impact of potential local discontinuities in the native segmentation (see Figure 2.4).

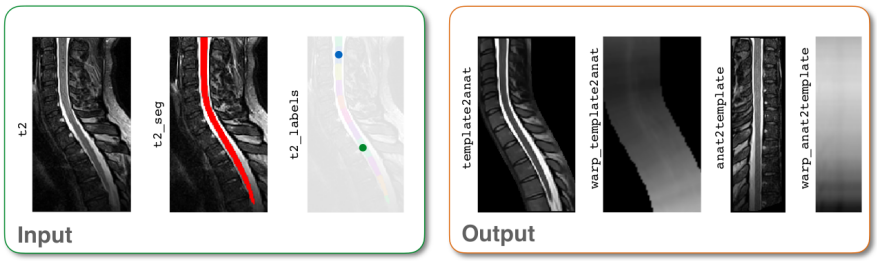

Figure 2.4: Registration of the PAM50 spinal cord template to the subject anatomical space.

2.3 Construction of Intramedullary Compartments

Starting from the template-derived cord mapped into subject space, the final intramedullary compartments were defined. The registered GM was binarized and subjected to light smoothing to ensure volumetric continuity, reducing potential voxel-wise irregularities introduced by the non-linear transformation. WM was then computed as the difference between the template-warped cord mask and the registered GM. The perimedullary compartment (CSF) was constructed through three-dimensional morphological dilation of the cord with a radius of three voxels, followed by subtraction of the original mask:

$$CSF = \text{dilate}(SC, r = 3) - SC$$

The three-voxel radius was kept constant for all subjects and represents an operational choice aimed at generating a continuous perimedullary shell around the cord. This parameter is not intended as a direct anatomical measurement of CSF thickness, but rather as a controlled approximation useful for constructing a coherent conductive domain for finite element modeling (see Figure 2.5). The final masks of cord, GM, WM, and CSF were saved in binary format in the native T2w space.

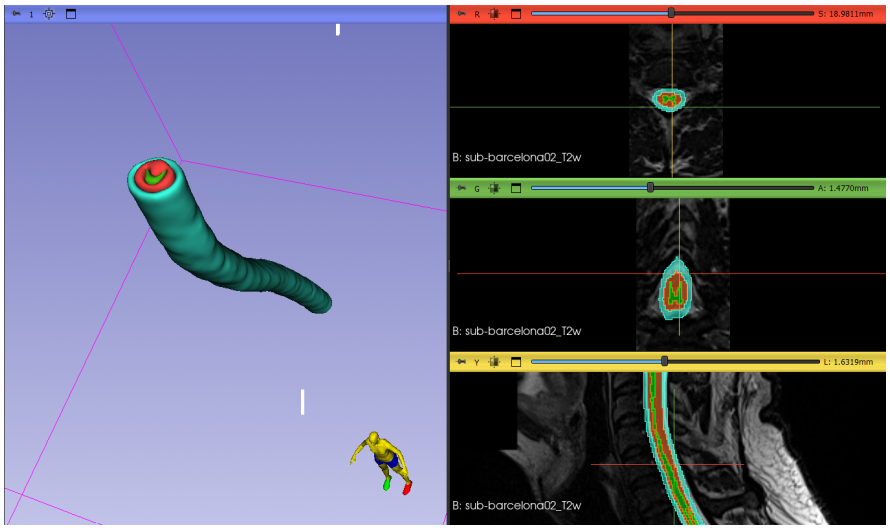

Figure 2.5: Construction of the perimedullary compartment by morphological dilation of the spinal cord and subtraction of the original mask.

2.4 Vertebral Segmentation and Geometric Benchmark

Vertebral structures were segmented by applying three different automatic frameworks to the T2w images in the subject's native space: TotalSegmentator (v1.5.7) [24], TotalSpineSegmentator (release 20260129) [20, 25], and SpinePS (development build 1.4.2.post2.dev0+54fb222) [26, 27]. Each software package was executed within dedicated `conda` environments. TotalSegmentator is based on nnU-Net [28]; TotalSpineSegmentator integrates nnU-Net segmentation with landmark-based vertebral labeling; SpinePS employs a two-stage pipeline including semantic segmentation and instance segmentation of vertebral levels. In addition to vertebrae, each framework produces a native spinal cord segmentation. Geometric metrics were computed from these segmentations in order to quantify inter-toolbox variability. Total volume was obtained by multiplying the number of segmented voxels by the voxel volume; cranio-caudal length was estimated as the extent of the mask along the z-axis; mean cross-sectional area (CSA) was calculated as the ratio between volume and length; the canal-to-cord ratio was derived from the respective labels; and the number of connected components was used as an index of segmentation continuity. All measurements were performed in the native T2w space.

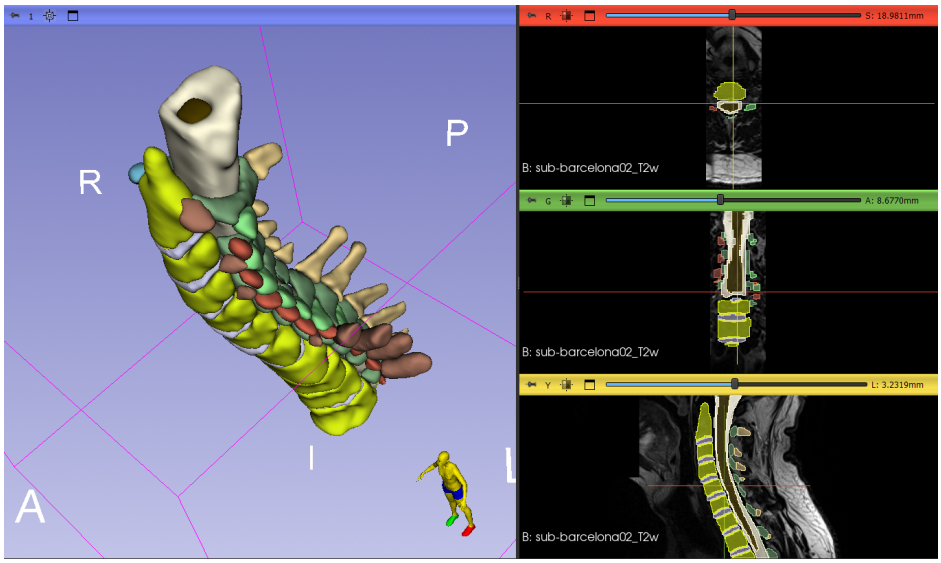

Figure 4.1 SpinePS

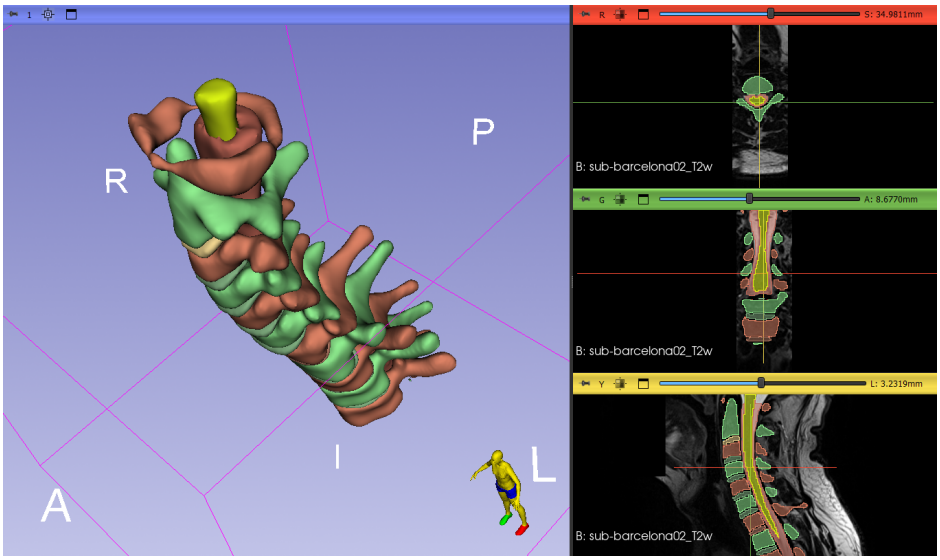

Figure 4.2 TotalSpineSegmentator

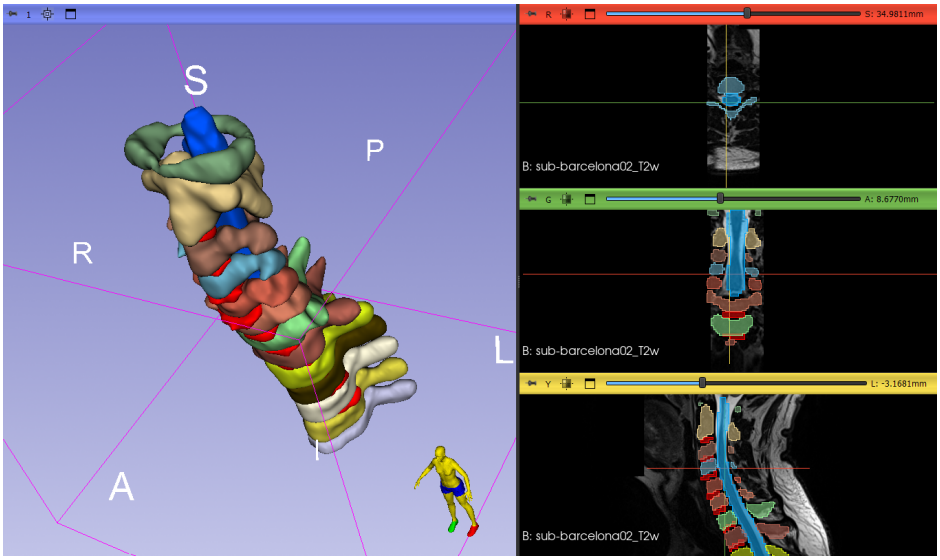

Figure 4.3 TotalSegmentator

Figure 2.6: Vertebral segmentations obtained for subject `sub_barcelona02`. Figure 4.1 shows the segmentation generated by SpinePS, Figure 4.2 by TotalSpineSegmentator, and Figure 4.3 by TotalSegmentator.

2.5 Integration for Computational Modeling

The benchmarking phase was kept separate from the construction of geometries for computational modeling. In the latter phase, the spinal cord segmentation derived from SCT was adopted as a common reference, independently of the toolbox used for vertebral segmentation. This choice is motivated by the documented sensitivity of FEM models to the geometric definition of anatomical compartments and their boundaries [29, 16].

For each subject, three distinct geometric configurations were therefore generated by combining the vertebrae segmented with each framework with the same cord and CSF segmentation derived from SCT. This procedure makes it possible to isolate the effect of vertebral segmentation on the overall geometry while keeping the intramedullary compartment constant.

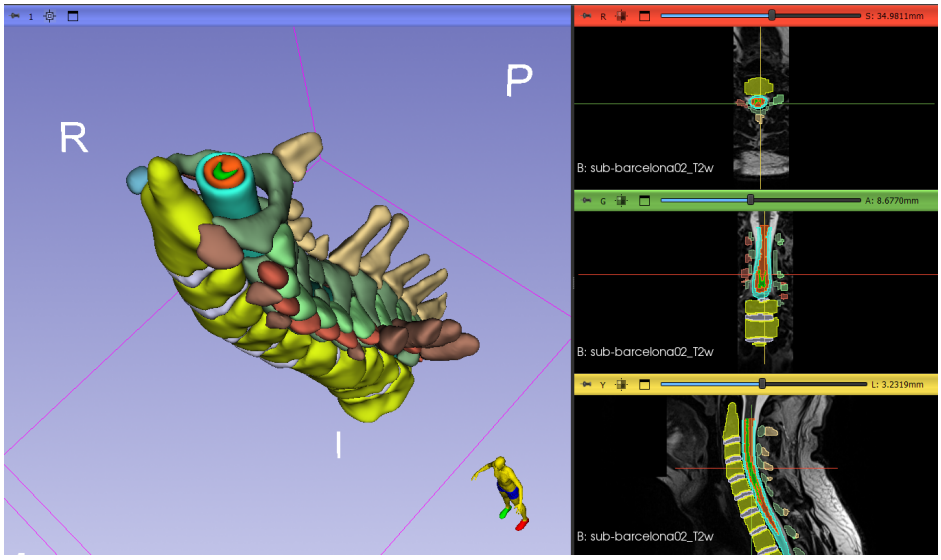

Figure 5.1 SCT + SpinePS

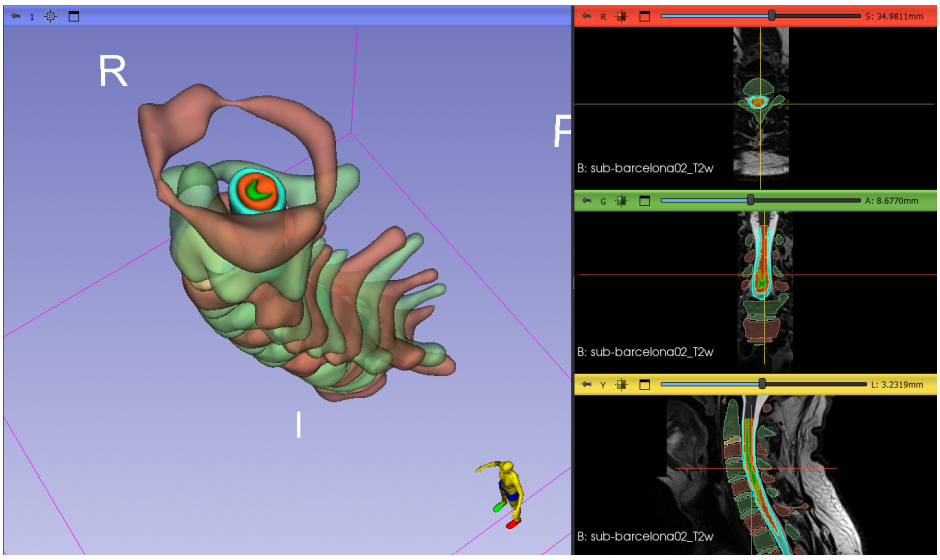

Figure 5.2 SCT + TotalSpineSegmentator

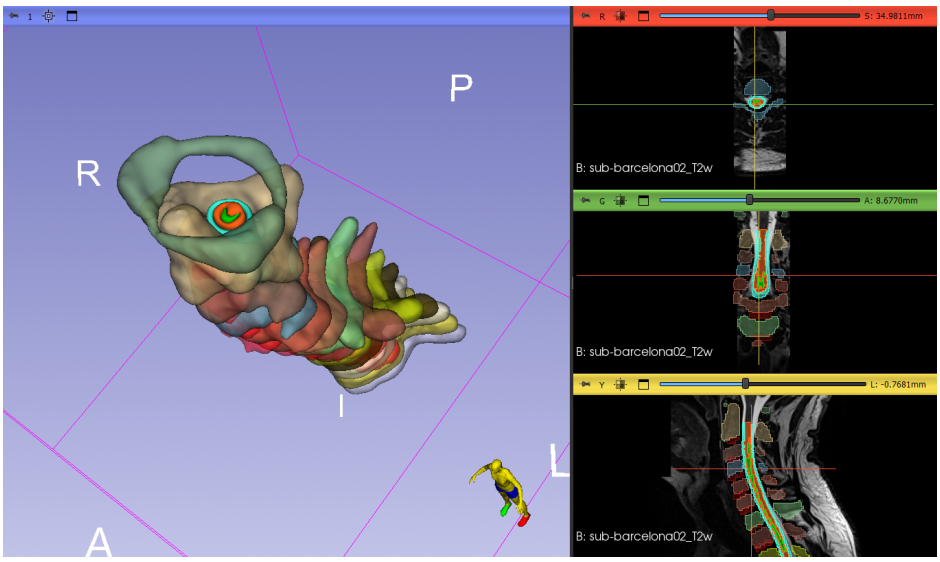

Figure 5.3 SCT + TotalSegmentator

Figure 2.7: Hybrid geometric configurations for subject `sub_barcelona02`. Each configuration combines the spinal cord and CSF segmentation obtained with SCT with vertebral structures segmented by a different framework: SpinePS (Figure 5.1), TotalSpineSegmentator (Figure 5.2), and TotalSegmentator (Figure 5.3).

Workflow Summary

For methodological clarity, the entire pipeline described in the previous sections is summarized in the block diagram shown in Figure 2.8. The figure outlines the operational workflow from dataset selection to the generation of the three final geometric configurations, highlighting the separation between the vertebral segmentation benchmarking phase and the integration phase for computational modeling.

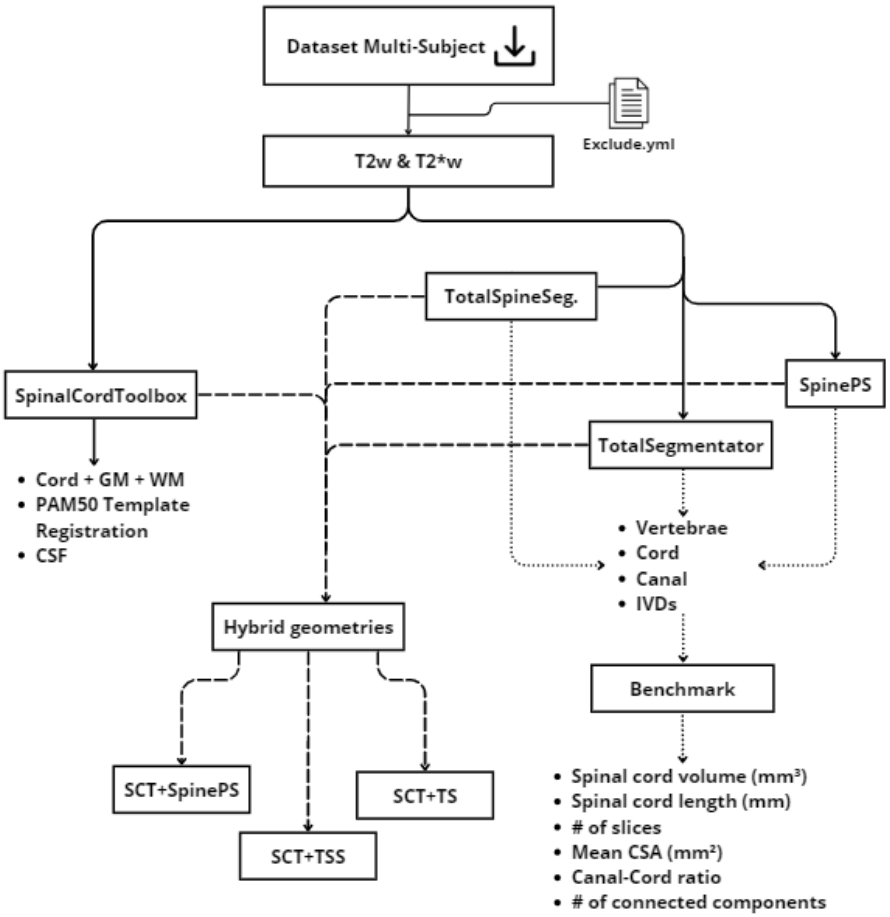

Figure 2.8: Summary diagram of the methodological pipeline: spinal cord segmentation with SCT and registration to PAM50 (branch A), vertebral segmentation with three toolboxes and geometric benchmark (branch B), and final integration for the generation of three geometric configurations intended for FEM modeling.

Chapter 3

Results

For each framework, the following parameters were quantified: spinal cord volume, cord length, number of occupied slices, mean CSA, canal-to-cord ratio, and number of connected components of the vertebral canal (see Table 3.1, 3.2, 3.3, 3.4).

SpinePS produced spinal cord volumes ranging from 12113 mm^3 to 15976 mm^3, with lengths between 177.0 mm and 205.5 mm and a number of occupied slices varying from 236 to 274. The mean CSA ranged from 59.16 mm^2 to 78.58 mm^2. The canal-to-cord ratio ranged between 2.39 and 3.04. In all subjects, a single connected component of the vertebral canal was identified. TotalSegmentator yielded volumes between 33012 mm^3 and 39757 mm^3, with lengths from 183.0 mm to 212.0 mm and a number of occupied slices between 183 and 212. The mean CSA ranged from 160.25 mm^2 to 217.23 mm^2. The canal-to-cord ratio was approximately 1.00 in all analyzed subjects. In this case as well, a single connected component of the canal was identified. TotalSpineSegmentator produced volumes between 11264 mm^3 and 14355 mm^3, with lengths ranging from 190.0 mm to 216.0 mm and a number of occupied slices between 190 and 216. The mean CSA ranged from 52.15 mm^2 to 66.77 mm^2. The canal-to-cord ratio ranged between 2.03 and 2.67. The number of connected components of the vertebral canal varied between 3 and 13 across subjects.

The quantitative comparison among the toolboxes reveals marked differences in volumetric and transverse parameters (volume and mean CSA), whereas longitudinal measures (length and number of occupied slices) show more limited variability across frameworks. In terms of spinal cord volume, TotalSegmentator yields significantly higher values than the other tools, with an average increase of approximately 166% relative to SpinePS. TotalSpine-

Segmentator, in contrast, shows slightly lower values compared to SpinePS (-6% on average). The comparison between SpinePS and SCT indicates a limited mean difference of approximately 3%. A similar trend is observed for mean CSA. TotalSegmentator presents average values approximately 163% higher than SpinePS, whereas TotalSpineSegmentator shows an average reduction of about 12%. SpinePS and SCT are substantially aligned, with differences below 5%. Regarding longitudinal measures, spinal cord length varies on average within 7 across tools, with maximum differences on the order of 10–15 mm in individual subjects. The number of occupied slices follows the same pattern, showing internal consistency with the segmented length. The canal-to-cord ratio highlights a marked divergence between TotalSegmentator and the other two toolboxes. SpinePS and TotalSpineSegmentator exhibit mean values between 2 and 3, whereas TotalSegmentator consistently remains around 1.00 (-63% relative to SpinePS). Finally, the number of connected components of the vertebral canal clearly differentiates TotalSpineSegmentator from the other tools: SpinePS and TotalSegmentator return a single connected component in all subjects, while TotalSpineSegmentator shows a mean of 8.75 components, with values ranging from 3 to 13.

Table 3.1: Geometric parameters obtained with SpinePS

Subject	vol_cord (mm^3)	length (mm)	slices	CSA (mm^2)	ratio canal/cord	n_comp canal
sub-barcelona02	15975.82	205.5	274	77.74	2.39	1
sub-amu01	13904.24	177.0	236	78.58	3.04	1
sub-brnoCeitec01	12915.79	182.25	243	70.88	2.67	1
sub-beijingPrisma01	12113.89	204.75	273	59.16	2.92	1

Table 3.2: Geometric parameters obtained with TotalSegmentator

Subject	vol_cord (mm^3)	length (mm)	slices	CSA (mm^2)	ratio canal/cord	n_comp canal
sub-barcelona02	37438.00	212.0	212	176.59	1.01	1
sub-amu01	39757.00	183.0	183	217.23	1.00	1
sub-brnoCeitec01	35921.29	190.0	190	189.06	1.01	1
sub-beijingPrisma01	33012.00	206.0	206	160.25	1.00	1

Table 3.3: Geometric parameters obtained with TotalSpineSegmentator

Subject	vol_cord (mm^3)	length (mm)	slices	CSA (mm^2)	ratio canal/cord	n_comp canal
sub-barcelona02	14355.00	215.0	215	66.77	2.03	3
sub-amu01	12647.00	190.0	190	66.56	2.67	13
sub-brnoCeitec01	12891.35	198.0	198	65.11	2.04	11
sub-beijingPrisma01	11264.00	216.0	216	52.15	2.40	8

Table 3.4: Geometric and tissue-specific parameters obtained with SCT

Subject	vol_cord (mm^3)	CSA_cord (mm^2)	vol_gm (mm^3)	vol_wm (mm^3)	CSA_gm (mm^2)	CSA_wm (mm^2)	gm/wm ratio
sub-barcelona02	15347	72.12	1345	6296	81.52	307.13	0.21
sub-amu01	13676	73.06	1130	6025	118.95	482.00	0.19
sub-brnoCeitec01	13155	66.85	1242	4826	124.25	321.75	0.26
sub-beijingPrisma01	11589	54.05	1116	4443	106.31	277.73	0.25

Chapter 4

Discussion

The results highlight structural differences among the segmentation frameworks that cannot be attributed to simple numerical variability. The discrepancies observed in volumetric and transverse parameters indicate that the toolboxes produce substantially different geometric representations of the spinal cord, rather than marginal variations of the same anatomical entity.

In this context, the agreement between SpinePS and SCT, both in terms of volume and mean CSA, suggests consistency in the definition of the anatomical boundaries of the spinal cord compartment. Considering that SCT represents a consolidated tool for quantitative spinal cord analysis, this alignment reinforces the reliability of the segmentations obtained with SpinePS in the analyzed sample. In contrast, TotalSegmentator shows a systematic overestimation of volume and CSA, associated with a canal-to-cord ratio close to unity. This configuration reflects a reduced distinction between contiguous anatomical compartments and a likely inclusion of perimedullary structures within the cord mask. Notably, the divergence does not concern longitudinal extent, which remains comparable across tools, but rather the transverse definition of the anatomical section. Consequently, the disagreement among frameworks appears to originate primarily from the criteria used to delineate the lateral borders of the cord, rather than from the identification of its cranio-caudal extent. TotalSpineSegmentator occupies an intermediate position from a dimensional perspective, showing volumes and CSA values closer to those of SpinePS and SCT; however, it introduces topological fragmentation of the vertebral canal, as indicated by the high number of connected components. This discontinuity is not evident in purely metric parameters, but becomes apparent through connectivity analysis, underscoring that dimensional evaluation alone is insufficient to characterize segmentation quality. Geometric continuity therefore assumes a central role in three-dimensional modeling and mesh generation processes. Taken together, these results show

that, starting from the same input images, different tools may produce divergent geometric configurations. The differences are mainly concentrated in transverse parameters and compartment definition, whereas longitudinal measures remain relatively stable. This pattern suggests that identification of the extension along the z-axis represents a more robust task than the accurate delineation of the lateral surfaces of the spinal cord.

In light of these findings, the choice of segmentation framework cannot be regarded as a purely technical aspect, but assumes direct methodological relevance in pipelines requiring geometric coherence and accurate distinction between anatomical compartments. A further implication concerns the generation of hybrid geometries, obtained by combining the cord and CSF segmentation derived from SCT with vertebral structures segmented by the different toolboxes. The differences observed in geometric parameters translate into distinct spatial configurations within the composite models. In particular, the volumetric overestimation associated with TotalSegmentator results in a reduction of the perimedullary space and a modification of the relative proportions among cord, CSF, and vertebral canal. Conversely, the canal fragmentation observed with TotalSpineSegmentator introduces discontinuities in the internal surface of the bony compartment, requiring post-processing interventions to restore geometric coherence. SpinePS, owing to the observed volumetric consistency and topological continuity, generates hybrid configurations characterized by more stable spatial relationships along the cranio-caudal axis. Ultimately, the behavior of the individual toolboxes affects not only the numerical values of geometric descriptors, but also determines structural differences in the construction of the three-dimensional geometries employed in subsequent stages of the pipeline. The quality and coherence of the segmentations are therefore reflected in the stability and plausibility of the generated hybrid configurations.

Chapter 5

Conclusions

In this work, a computational pipeline was developed and validated for the generation of three-dimensional spinal cord models from multi-contrast MRI images. The integration of automatic segmentation, anatomical normalization to the PAM50 template, and reconstruction of vertebral structures within a unified spatial reference system enabled the generation of coherent binary volumes of gray matter, white matter, cerebrospinal fluid, and vertebrae, directly applicable to finite element numerical modeling. The application of the pipeline to a heterogeneous multicenter dataset demonstrated the robustness of the framework with respect to inter-site variability and acquisition differences. The combined use of T2 and T2* contrasts, vertebral initialization during registration, and application of the inverse template transformation ensured anatomical coherence along the cranio-caudal axis and geometric continuity across segmented compartments. The resulting geometries satisfy the consistency requirements necessary for mesh generation and for the execution of volume conduction simulations. The benchmark among different segmentation toolboxes further demonstrated that distinct algorithmic choices may produce substantially divergent geometric configurations from the same input images. In particular, the main discrepancies are concentrated in transverse parameters and in compartment definition, with direct implications for the construction of hybrid geometries. This finding highlights the methodological role of segmentation within the pipeline and the need for critical evaluation of the frameworks employed when the ultimate goal is electrophysiological modeling.

Among possible future developments, a priority is the systematic quantification of the impact of geometric variations on numerical simulation outcomes. A sensitivity analysis introducing controlled variations in spinal cord CSA or CSF thickness would allow assessment of how segmentation differences propagate into potential distribution and electric fields estimated

through FEM. In parallel, further investigation of mesh quality generated from different geometries would enable direct correlation between segmentation characteristics and numerical parameters such as element regularity, presence of degenerate elements, and solution stability.

Overall, this work provides a reproducible methodological foundation that explicitly links anatomical segmentation and electrophysiological modeling, defining an operational framework for neuromodulation studies in macroscopically preserved sublesional segments of Spinal Cord Injury. The formalization of this workflow represents a step toward more systematic integration between quantitative imaging and numerical simulation in the field of neuroengineering.

List of Figures

Bibliography

[1] Y. Lu, Z. Shang, W. Zhang, X. Hu, R. Shen, K. Zhang, Y. Zhang, L. Zhang, B. Liu, M. Pang, and L. Rong, "Global, regional, and national burden of spinal cord injury from 1990 to 2021 and projections for 2050: A systematic analysis for the global burden of disease 2021 study," *Ageing Research Reviews*, vol. 103, p. 102598, 2025.

[2] A. Anjum, M. D. Yazid, M. Fauzi Daud, J. Idris, A. M. H. Ng, A. Selvi Naicker, O. H. R. Ismail, R. K. Athi Kumar, and Y. Lokanathan, "Spinal cord injury: Pathophysiology, multimolecular interactions, and underlying recovery mechanisms," *International Journal of Molecular Sciences*, vol. 21, no. 20, 2020.

[3] M. Kim, W. Jeong, S. Jang, J. H. Park, Y. Bae, and S. W. Lee, "Spinal cord injury epidemiology and causes: A worldwide analysis with 2050 projections," *Healthcare*, vol. 13, no. 20, 2025.

[4] Y. Liu, X. Yang, Z. He, J. Li, Y. Li, Y. Wu, A. Manyande, M. Feng, and H. Xiang, "Spinal cord injury: global burden from 1990 to 2019 and projections up to 2030 using bayesian age-period-cohort analysis," *Frontiers in Neurology*, vol. Volume 14 - 2023, 2023.

[5] M. Mackiewicz-Milewska, M. Cisowska-Adamiak, I. Głowacka-Mrotek, and H. Mackiewicz-Nartowicz, "Traumatic vs. non-traumatic spinal cord injury—epidemiology, complications, and neurological status during rehabilitation," *Journal of Clinical Medicine*, vol. 14, no. 15, 2025.

[6] J. Ditunno, "American spinal injury standards for neurological and functional classification of spinal cord injury: past, present and future. 1992 heiner sell lecture of the american spinal injury association.," *The Journal of the American Paraplegia Society*, vol. 17 1, pp. 7–11, 1994.

[7] S. Harkema, Y. Gerasimenko, J. Hodes, J. Burdick, C. Angeli, Y. Chen, C. Ferreira, A. Willhite, E. Rejc, R. G. Grossman, *et al.*, "Effect of

epidural stimulation of the lumbosacral spinal cord on voluntary movement, standing, and assisted stepping after motor complete paraplegia: a case study," *The Lancet*, vol. 377, no. 9781, pp. 1938–1947, 2011.

[8] M. L. Gill, P. J. Grahn, J. S. Calvert, M. B. Linde, I. A. Lavrov, J. A. Strommen, L. A. Beck, D. G. Sayenko, M. G. Van Straaten, D. I. Drubach, D. D. Veith, A. R. Thoreson, C. Lopez, Y. P. Gerasimenko, V. R. Edgerton, K. H. Lee, and K. D. Zhao, "Neuromodulation of lumbosacral spinal networks enables independent stepping after complete paraplegia," *Nature medicine*, vol. 24, p. 1677—1682, November 2018.

[9] J. S. Calvert, P. J. Grahn, J. A. Strommen, I. A. Lavrov, L. A. Beck, M. L. Gill, M. B. Linde, D. A. Brown, M. G. Van Straaten, D. D. Veith, C. Lopez, D. G. Sayenko, Y. P. Gerasimenko, V. R. Edgerton, K. D. Zhao, and K. H. Lee, "Electrophysiological guidance of epidural electrode array implantation over the human lumbosacral spinal cord to enable motor function after chronic paralysis," *Journal of Neurotrauma*, vol. 36, no. 9, pp. 1451–1460, 2019. PMID: 30430902.

[10] A. Rowald, S. Komi, R. Demesmaeker, E. Baaklini, S. D. Hernandez-Charpak, E. Paoles, H. Montanaro, A. Cassara, F. Becce, B. Lloyd, *et al.*, "Activity-dependent spinal cord neuromodulation rapidly restores trunk and leg motor functions after complete paralysis," *Nature medicine*, vol. 28, no. 2, pp. 260–271, 2022.

[11] E. Formento, K. Minassian, F. Wagner, J. B. Mignardot, C. G. Le Goff-Mignardot, A. Rowald, J. Bloch, S. Micera, M. Capogrosso, and G. Courtine, "Electrical spinal cord stimulation must preserve proprioception to enable locomotion in humans with spinal cord injury," *Nature neuroscience*, vol. 21, no. 12, pp. 1728–1741, 2018.

[12] J. Ladenbauer, K. Minassian, U. S. Hofstoetter, M. R. Dimitrijevic, and F. Rattay, "Stimulation of the human lumbar spinal cord with implanted and surface electrodes: A computer simulation study," *IEEE Transactions on Neural Systems and Rehabilitation Engineering*, vol. 18, no. 6, pp. 637–645, 2010.

[13] M. Capogrosso, N. Wenger, S. Raspopovic, P. Musienko, J. Beauparlant, L. B. Luciani, G. Courtine, and S. Micera, "A computational model for epidural electrical stimulation of spinal sensorimotor circuits," *Journal of Neuroscience*, vol. 33, no. 49, pp. 19326–19340, 2013.

[14] B. Coburn and W. Sin, "A theoretical study of epidural electrical stimulation of the spinal cord part i: finite element analysis of stimulus fields," *IEEE Transactions on Biomedical Engineering*, vol. 32, no. 10, pp. 971–977, 1985.

[15] F. Rattay, K. Minassian, and M. R. Dimitrijevic, "Epidural electrical stimulation of posterior structures of the human lumbosacral cord: 2. quantitative analysis by computer modeling," *Spinal Cord*, vol. 38, pp. 473–489, 2000.

[16] J. Ladenbauer, K. Minassian, U. S. Hofstoetter, M. R. Dimitrijevic, and F. Rattay, "Stimulation of the human lumbar spinal cord with implanted and surface electrodes: A computer simulation study," *IEEE Transactions on Neural Systems and Rehabilitation Engineering*, vol. 18, no. 6, pp. 637–645, 2010.

[17] N. Khadka, X. Liu, H. Zander, J. Swami, E. Rogers, S. F. Lempka, and M. Bikson, "Realistic anatomically detailed open-source spinal cord stimulation (rado-scs) model," *Journal of Neural Engineering*, vol. 17, p. 026033, apr 2020.

[18] S. Garg and S. I. R. Bhagyashree, "Spinal cord mri segmentation techniques and algorithms: A survey," *SN Computer Science*, vol. 2, 2021.

[19] B. De Leener, S. Lévy, S. M. Dupont, V. S. Fonov, N. Stikov, D. Louis Collins, V. Callot, and J. Cohen-Adad, "Sct: Spinal cord toolbox, an open-source software for processing spinal cord mri data," *NeuroImage*, vol. 145, pp. 24–43, 2017.

[20] Y. Warszawer, N. Molinier, J. Valosek, P.-L. Benveniste, S. Bédard, E. Shirbint, F. Mohamed, C. Tsagkas, S. Kolind, L. Lynd, J. Oh, A. Prat, R. Tam, A. Traboulsee, S. Patten, L. E. Lee, A. Achiron, and J. Cohen-Adad, "Totalspineseg: Robust spine segmentation with landmark-based labeling in mri," *ResearchGate preprint*, 2025.

[21] E. A. Rashed, J. Gomez-Tames, and A. Hirata, "Influence of segmentation accuracy in structural mr head scans on electric field computation for tms and tes," *arXiv preprint*, 2020.

[22] J. Cohen-Adad, E. Alonso-Ortiz, M. Abramovic, C. Arneitz, N. Atcheson, L. Barlow, R. L. Barry, M. Barth, M. Battiston, C. Büchel, M. Budde, V. Callot, A. J. Combes, B. De Leener, M. Descoteaux, P. Loureiro de Sousa, M. Dostál, J. Doyon, A. Dvorak, F. Eippert,

K. R. Epperson, K. S. Epperson, P. Freund, J. Finsterbusch, A. Foias, M. Fratini, I. Fukunaga, C. A. Gandini Wheeler-Kingshott, G. Germani, G. Gilbert, F. Giove, C. Gros, F. Grussu, A. Hagiwara, P.-G. Henry, T. Horák, M. Hori, J. Joers, K. Kamiya, H. Karbasforoushan, M. Keřkovský, A. Khatibi, J.-W. Kim, N. Kinany, H. Kitzler, S. Kolind, Y. Kong, P. Kudlička, P. Kuntke, N. D. Kurniawan, S. Kusmia, R. Labounek, M. M. Laganà, C. Laule, C. S. Law, C. Lenglet, T. Leutritz, Y. Liu, S. Llufriu, S. Mackey, E. Martinez-Heras, L. Mattera, I. Nestrasil, K. P. O'Grady, N. Papinutto, D. Papp, D. Pareto, T. B. Parrish, A. Pichiecchio, F. Prados, Rovira, M. J. Ruitenberg, R. S. Samson, G. Savini, M. Seif, A. C. Seifert, A. K. Smith, S. A. Smith, Z. A. Smith, E. Solana, Y. Suzuki, G. Tackley, A. Tinnermann, J. Valošek, D. Van De Ville, M. C. Yiannakas, K. A. Weber, N. Weiskopf, R. G. Wise, P. O. Wyss, and J. Xu, "Spine generic public database (multi-subject)," Nov. 2020.

[23] A. Oliver-Taylor, A. Li, A. Thomas, A. Flinker, A. S. Wagner, A. Karakuzu, A. Zazio, A. Nikolaidis, A. Lazari, A. de la Vega, A. Giacomel, A. Rockhill, A. Jones, A. L. Cohen, A. von Lautz, A. D'Astous, A. Gramfort, A. Hutton, A. Routier, A. Foias, A. Khan, A. Wickenheiser, A. Dai, A. R. Hopkins, A. Fouto, A. Eklund, A. Pigorini, A. Hoopes, A. Jahn, A. Janke, A. Sólon, A. Galassi, A. Sala, A. Rokem, A. Stolk, A. Jahanpour, A. Delorme, A. Marcoux, A. Basavaraj, A. G. Gillman, A. Monika Mowinckel, A. Vrolijk, A. Gunduz, A. Adebimpe, B. N. Nichols, B. Kincses, B. Beasley, B. Dichter, B. Gagl, B. Thirion, B. Clénet, B. Voytek, B. McPherson, B. L. Foster, B. A. Wandell, B. N. Lundstrom, C. Maumet, C. Miniussi, C. Madjar, C. Pasturel, C. Benjamin, C. Gahnström, C. Holdgraf, C. J. Gorgolewski, C. Rorden, C. Büchel, C. Horea, C. Rogers, C. Phillips, C. G. Schwarz, C. J. Honey, C. J. Markiewicz, C. Lee-Messer, C. Moreau, C. Hansen, C. Baker, C. Pernet, C. Eierud, D. Sturgeon, D. Brady, D. Levitas, D. Lurie, D. A. Handwerker, D. McCloy, D. Alsop, D. Boas, D. Groppe, D. Keator, D. McAlpine, D. Thomas, D. Draschkow, D. Oathes, D. Patterson, D. Papadopoulos Orfanos, D. Petrov, D. Hermes, D. Huijser, D. Jarecka, D. N. Greve, D. Macleod, D. Truong, D. Moraczewski, D. Nielson, E. Ort, E. Marcantoni, E. Bock, E. DuPre, E. Warmerdam, E. Karaca, E. A. Earl, E. Achten, E. Bridgeford, E. W. Dickie, E. Blackwood, E. P. Duff, E. Mikulan, F. Raimondo, F. Orihuela-Espina, F. Alfaro Almagro, F. Szczepankiewicz, F. Maria Castelli, F. Pestilli, F. W. Feingold, F. Tadel, F. Breuer, G. Rizzo, G. Chen, G. Varoquaux, G. Vaillant, G. Bertazzoli, G. Guidali, G. Mazzamuto, G. de Hollander,

G. Piantoni, G. Nordio, G. M. Knudsen, G. Castegnaro, G. Gallitto, G. Searle, G. J. Matheson, G. Kiar, G. Noack, G. Gilmore, G. Flandin, G. Niso, G. Schaefer, G. Nilsonne, H. Innes-Brown, H. D. Hansen, H. Lu, H.-T. Wang, H. Cockx, H. Mutsaerts, H. Ombao, H. Boniface, I. Isik, I. Lipp, I. Neuroinformatics Coordinating Facility, I. Groen, I. To, I. Staden, J. von der Aar, J. Sanz-Robinson, J. Kaczmarzyk, J. Gholam, J. Kent, J. Mathijs Schoffelen, J. Petr, J. Valosek, J.-M. Schoffelen, J.-B. Poline, J.-C. Mariani, J.-C. Houde, J.-D. Gallezot, J.-P. Lachaux, J. Mumford, J. Casimir, J. G. Ojemann, J. S. Grethe, JegouA, J. Dalenberg, J. Moreau, J. A. Turner, J. Rieger, J. Detre, J. Pellman, J. T. Wodder, J. Durnez, J. Haitz Legarreta Gorroño, J. C. Lau, J. Winawer, J. Kuijer, J. Manuel Saborit, J. Wexler, J. Woods, J. Sprenger, J.-K. Pfarr, J. Cohen-Adad, J. C Hernandez Pavon, J. Welzel, J. Fouquet, K. Gunalan, K. J. Miller, K. Lee, K. Heuer, K. Robbins, K. Larcher, K. Ray, K. Whitaker, K. Gregorova, K. Gramann, K. Thielemans, K. Bouchard, K. Schilling, L. Fesselier, , L. John Arnold Foundation, L. Beltrachini, L. Kamentsky, L. Walger, L. Wittkuhn, L. Hamilton, L. Pollonini, L. Hernandez-Garcia, L. J. Edwards, L. Zehl, M. Jas, M. Biabani, M. Narayan, M. Mercier, M. Yaqub, M. Lalancette, M. Castellaro, M. Ermolova, M. de la Iglesia, M.-E. Picard, M.-H. Bourget, M. Mikkelsen, M. Morawski, M. Bortoletto, M. Craig, M. Noergaard, M. Szinte, M. Wilson, M. Bulgari, M. Miedema, M. Pawlik, M. Goncalves, M. Boudreau, M. Dugré, M. Guay-Paquet, M. Cieslak, M. Sanderson, M. Stead, M. Tonietto, M. Günther, M. Van Osch, M. Chourrout, M. Veronese, M. J Shader, M. Pasternak, M. A. van den Boom, M. Ganz-Benjaminsen, M. Kline Struhl, M. Chappell, M. Firbank, M. Hanke, M. P. Harms, M. P. Milham, M. P. Notter, M. Schirner, M. Wang, M. Naveau, M. Torabi, M. Denissen, M. Bilgel, N. Pouratian, N. Petridou, N. Rotstein, N. Institute of Mental Health, N. Hardcastle, N. Holmes, N. Traut, N. F. Ramsey, N. Guenther, N. C. Swann, N. Rogasch, N. Bhagwat, N. Beliy, N. Bigdely Shamlo, O. David, O. Devinsky, O. Esteban, P. LaMontagne, P. Sethi, P. Clement, P. Park, P. Wighton, P.-J. Toussaint, P. Herholz, P. Ritter, P. Najafi, P. Rioux, P. Vandemaele, P. Reddy Raamana, Q. Chu, R. Cameron Craddock, R. Gupta, R. Gau, R. Höchenberger, R. N. Henson, R. B. Innis, R. E. Smith, R. Knight, R. Luke, R. Oostenveld, R. Guidotti, R. Toro, R. Goyal, R. W. Blair, R. A. Poldrack, R. Adon, S. Das, S. Garcia, S. Guay, S. Le Meur-Diebolt, S. Nastase, S. Elgayar, S. D'Ambrosio, S. S. Ghosh, S. Makeig, S. Urchs, S. Jeung, S. Y. Shirazi, S. Bansal, S. Wang, S. Isabella, S. B. Vos, S. Hayashi, S. Kulkarni, S. Appelhoff, S. De Smet, S. Moia, S. Bickel, S. Meisler, S. Bhogawar, S. Bail-

let, S. Takerkart, S. Tourbier, S. Grothkopp, T. Pal Attia, T. Yarkoni, T. Spisak, T. Józsa, T. Khuhn, T. Salo, T. L. Brooks, T. Deffieux, T. E. Nichols, T. Funck, T. Kirk, T. Okell, T. Wachtler, T. Auer, T. Ole Bergmann, T. Dickscheid, T. Berg, T. Betthauser, T. Bengfort, T. Hampshire, T. Wager, T. Stöter, T. Riddle, T. Glatard, T. Collins, U. Bingel, V. Sochat, V. Raguram, V. H. Souza, V. D. Calhoun, V. Iacovella, V. Siless, V. Litvak, W. van der Zwaag, W. Clarke, W. Triplett, W. V. Potters, X. Li, Y. O. Halchenko, Y. Balbastre, Y. Ashar, Y. Wang, Z. Michael, Z.-D. Deng, ezemikulan, josator2, monkeyman192, patrick-g h, and Bergeron, "The brain imaging data structure (bids) specification," Feb. 2026.

[24] J. Wasserthal, H.-C. Breit, M. T. Meyer, M. Pradella, D. Hinck, A. W. Sauter, T. Heye, D. T. Boll, J. Cyriac, S. Yang, M. Bach, and M. Segeroth, "Totalsegmentator: Robust segmentation of 104 anatomic structures in ct images," *Radiology: Artificial Intelligence*, vol. 5, no. 5, p. e230024, 2023.

[25] Y. Warszawer, N. Molinier, J. Valošek, E. Shirbint, P.-L. Benveniste, A. Achiron, A. Eshaghi, and J. Cohen-Adad, "Fully automatic vertebrae and spinal cord segmentation using a hybrid approach combining nnu-net and iterative algorithm," in *ISMRM & ISMRT annual Meeting & Exhibition*, November 2024.

[26] H. Möller, R. Graf, J. Schmitt, B. Keinert, H. Schön, M. Atad, A. Sekuboyina, F. Streckenbach, F. Kofler, T. Kroencke, S. Bette, S. N. Willich, T. Keil, T. Niendorf, T. Pischon, B. Endemann, B. Menze, D. Rueckert, and J. S. Kirschke, "SPINEPS—automatic whole spine segmentation of t2-weighted MR images using a two-phase approach to multi-class semantic and instance segmentation,"

[27] R. Graf, J. Schmitt, S. Schlaeger, H. K. Möller, V. Sideri-Lampretsa, A. Sekuboyina, S. M. Krieg, B. Wiestler, B. Menze, D. Rueckert, *et al.*, "Denoising diffusion-based mri to ct image translation enables automated spinal segmentation," *European Radiology Experimental*, vol. 7, no. 1, p. 70, 2023.

[28] F. Isensee, P. F. Jaeger, S. A. A. Kohl, J. Petersen, and K. H. Maier-Hein, "nnu-net: a self-configuring method for deep learning-based biomedical image segmentation," *Nature Methods*, vol. 18, no. 2, pp. 203–211, 2021.

[29] M. Capogrosso, N. Wenger, S. Raspopovic, P. Musienko, J. Beauparlant, L. Bassi Luciani, G. Courtine, and S. Micera, "A computational model for epidural electrical stimulation of spinal sensorimotor circuits," *Journal of Neuroscience*, vol. 33, no. 49, pp. 19326–19340, 2013.